

Papanicolaou Stain Unmixing for RGB Image Using Weighted Nucleus Sparsity and Total Variation Regularization

Nanxin Gong^{a,*}, Saori Takeyama^a, Masahiro Yamaguchi^a, Takumi Urata^a, Fumikazu Kimura^b, Keiko Ishii^c

^a *Institute of Science Tokyo, Yokohama, Kanagawa, Japan*

^b *Shinshu University, Matsumoto, Nagano, Japan*

^c *Okaya City Hospital, Okaya, Honcho, Nagano, Japan*

Abstract

The Papanicolaou stain, consisting of eosin Y, hematoxylin, light Green SF yellowish, orange G, and Bismarck brown Y, provides extensive color information essential for cervical cancer screening in cytopathology. However, the visual observation of these colors is subjective and difficult to characterize. In digital image analysis, the RGB intensities are affected by staining and imaging variations, hindering direct quantification of color in Papanicolaou-stained samples. Stain unmixing is a promising alternative that quantifies the amounts of dyes. In previous work, multispectral imaging was utilized to estimate the dye amounts of Papanicolaou stain for quantitative diagnosis. Still, its application to RGB images presents a challenge since the number of dyes exceeds the three RGB channels. This paper proposes a novel Papanicolaou stain unmixing method for RGB images that incorporates three key assumptions: nonnegative stain abundances; a sparse spatial distribution of hematoxylin, which binds to nuclei; and piecewise smoothness of stain abundances. By formulating this as an optimization problem with nonnegativity, weighted nucleus sparsity, and total variation regularizations, our method achieved excellent performance in stain quantification when validated against the results of multispectral imaging. We also adopted the proposed method for discriminating lobular endocervical glandular hyperplasia (LEGH), a precancerous lesion of gastric-type adenocarcinoma of the cervix. The resulting quantification distinctly characterized differences between LEGH and normal endocervical cells with stain abundance, and a classifier based on the quantification results achieved 98.0% accuracy. This demonstrates the significant potential of RGB-based stain unmixing for quantitative diagnosis.

Keywords: Color deconvolution, Cytopathology, Lobular endocervical glandular hyperplasia, Papanicolaou stain, Stain unmixing.

1. Introduction

Histopathology, involving the microscopic examination of tissue sections, is crucial for definitive cancer diagnosis, grading, and staging. Cytopathology, focusing on the analysis of exfoliated cells, is widely used for minimally invasive diagnostic procedures (Jenkins, 2007). Cytopathology plays a key role in early cancer detection (e.g., cervical cancer screening). Through the Pap smear, cervical cells are collected and stained with the Papanicolaou stain, which discriminates cellular components by staining nuclei with hematoxylin (H), lipids with Bismarck brown Y (BY), and cytoplasm with Eosin Y (EY), Light Green SF yellowish (LG), and Orange G (OG), with intensity depending on factors like molecular weight, diffusivity, and differentiation.

Although the color in Papanicolaou stain is important in differentiating nuclei and cytoplasm of different types of cells, its visual characterization is often subjective and challenging to articulate. The application of digital image analysis is a potential solution for this purpose, and several methods have been proposed to quantify the colors of Papanicolaou-stained cytological specimen images. For instance, Kai et al., (1999) and Nunobiki et al., (2002) introduced quantitative and qualitative analyses of stain color in RGB color spaces, while Sakamoto et al., (1998) quantified variations in cytoplasmic

* Corresponding author.

E-mail address: gong.n.aa@m.titech.ac.jp (Nanxin Gong).

colors in the CIELAB color space. However, the color in digital pathology imaging is affected by variations in staining processes and imaging devices (Yagi, 2011). Although color normalization and color augmentation techniques have been proposed, quantification based on physical quantities directly linked to the staining properties offers a distinct advantage over psychophysical quantities based on visual appearance.

As a method to quantify colors using a physical quantity, estimating the stain abundance or dye amount based on spectral imaging has been proposed (Abe et al., 2005; Fujii et al., 2002). As for the application to the Papanicolaou stain, our prior research developed a dye amount estimation method based on 14-band multispectral (MS) images capturing Papanicolaou-stained specimens (Takeyama et al., 2025). This method employed MS images to estimate the dye amount in each pixel of cytological specimens via the pseudoinverse matrix that consists of the spectral absorption coefficients. However, MS cameras are not common in pathological imaging and require a lengthy scanning process. Therefore, it is expected to utilize RGB images in practice, which can be quickly scanned through a whole slide image (WSI) scanner (Weinstein et al., 2009).

Ruifrok et al., (2001) introduced a color deconvolution (CD) method to unmix RGB images into up to three dyes in converted optical density (OD) space, utilizing the OD vectors of pure dyes. This approach assumes that the absorbance at each pixel is a linear combination of these dyes, and it computes the abundance of each dye by multiplying the observed OD values with the inverse of the stain OD matrix. This method is widely adopted in digital pathology. However, when more than three dyes are involved, such as the Papanicolaou stain, the linear system becomes ill-posed. Moreover, nonnegative matrix factorization (NMF) has been adopted in an unsupervised stain unmixing framework, where both the stain color vectors and the corresponding stain abundances are simultaneously estimated for each image (Rabinovich et al., 2003). Vahadane et al., (2016) enhanced NMF by introducing a sparsity constraint, extending it to sparse NMF (SNMF), which preserves biological structure information during stain unmixing. Nevertheless, when the number of dyes exceeds the available image channels, obtaining suitable stain vectors becomes difficult, often resulting in multiple valid but distinct solutions. Addressing the problem typically requires prior spectral knowledge to mitigate ambiguities (McRae et al., 2019).

Other popular stain separation methods include independent component analysis (ICA) (Trahearn et al., 2015), singular value decomposition (SVD) (Macenko et al., 2009), blind color deconvolution (BCD) (Gavrilovic et al., 2013), adaptive color deconvolution (ACD) (Zheng et al., 2019), and Bayesian K-SVD (Pérez-Bueno et al., 2022). These approaches typically focus on estimating the stain matrix, while the stain abundance is often computed using conventional CD. Due to limited research in this area, accurately unmixing more than three dyes from three-channel RGB images remains a major challenge.

A group sparsity model-based algorithm has been proposed for unmixing more than three dyes in brightfield multiplex immunohistochemistry (IHC) images, but its applicability is limited to specific dyes due to reliance on biomarker co-localization (Chen and Srinivas, 2015). Although recent studies have demonstrated the feasibility of deep learning-based stain decomposition for IHC images when the number of biomarkers exceeds the number of imaging channels (Abousamra et al., 2023; Fassler et al., 2020), the primary objective in IHC remains the detection and spatial localization of individual biomarkers rather than precise quantification of their abundance. Moreover, to simplify the decomposition process, many methods assume mutually exclusive or minimally overlapping expression of different biomarkers. These assumptions do not hold in Papanicolaou staining, where multiple dyes frequently coexist within the same pixel, resulting in more complex color mixing patterns.

Rather than concentrating on RGB imaging, we find related advancements in hyperspectral imaging, specifically in the field of spectral unmixing within remote sensing. Spectral unmixing aims to identify the reference spectra, quantify their spectral signatures, and compute their fractional abundances using observed mixed hyperspectral vectors (Keshava and Mustard, 2002). Although hyperspectral images hold numerous channels, linear spectral unmixing often needs to be approached as a sparse regression problem, utilizing known spectra from an existing library (Iordache et al., 2011). The Sparse Unmixing via Variable Splitting and Augmented Lagrangian (SUnSAL) algorithm evaluates sparsity in the spectral domain using the l_1 norm of the abundance matrix (Bioucas-Dias and Figueiredo, 2010). SUnSAL-TV further enhances this model by integrating total variation (TV) regularization, which promotes smoothness across neighboring pixels (Iordache et al., 2012). Subsequent methods, such as those based on re-weighted regularizers (DRSU-TV) (Wang et al., 2017) or spectral-spatial penalty terms as in the Spectral-spatial Weighted Sparse Unmixing (S2WSU) (Zhang et al., 2018), further enhance sparsity by introducing weights to the sparsity term.

Although the specific problem differs, optimization-based unmixing methods with sparsity constraints may still be effective for Papanicolaou stain, particularly in cases where the number of dyes exceeds the number of RGB channels. However, the common assumption of endmember sparsity in hyperspectral unmixing is not appropriate for Papanicolaou-stained images, where almost all endmembers (i.e., dyes) are typically present in the image. This limitation motivates the design of a new sparsity constraint tailored to the characteristics of Papanicolaou staining.

Therefore, in this study, we propose an optimization-based stain unmixing method for Papanicolaou-stained RGB images, incorporating prior knowledge of stain abundance characteristics. Specifically, the method leverages the following three properties:

- **Nonnegativity:** At any given pixel, stain abundance and its corresponding OD value must be nonnegative. Negative values would suggest an unrealistic emission of light.
- **Nucleus sparsity:** In Pap-stained samples, hematoxylin (H) typically binds to nuclei, whereas the cytoplasm is nearly unstained by H. To reflect this distribution, we introduce a sparsity-promoting regularization term that iteratively assigns higher weights to pixels with lower H abundance and lower weights to higher H abundance, thereby enhancing sparsity in non-nuclear regions while preserving signal in nuclei.
- **Piecewise smoothness:** Due to the continuity of cellular structures, stain abundances are expected to vary smoothly within homogeneous regions. We model this property using TV regularization to encourage spatial coherence among neighboring pixels.

In stain unmixing experiments, obtaining ground truth for stain matrix and stain abundances presents significant challenges. Traditional methods often rely on manually selecting representative stained regions, which can introduce subjective bias. To mitigate this, we prepared single-stain specimens to compute the stain matrix. Additionally, following the methodology of (Takeyama et al., 2025), we utilized MS stain unmixing results as ground truth. This approach is justified because the number of spectral channels in MS imaging exceeds the number of dyes used in Papanicolaou staining, resulting in an overdetermined system. Furthermore, we conducted benchmark comparisons between our proposed method and existing stain unmixing algorithms to evaluate performance in stain quantification.

To further validate the applicability of our stain unmixing method, we applied it to quantify the colors of the cytoplasmic mucin in normal endocervical (EC) cells and lobular endocervical glandular hyperplasia (LEGH) cells. LEGH is a benign glandular tumor of the uterine cervix reported in (Nucci et al., 1999). As it is considered a precursor lesion of gastric-type endocervical adenocarcinoma, early detection and accurate diagnosis of LEGH is of great significance for a good prognosis. Despite its importance, LEGH cells lack nuclear atypia, and it is difficult to distinguish them from EC cells morphologically by human eyes (Kanai et al., 2020; Nucci, 2014). According to (Ishii, 2001; Ishii et al., 1999; Kimura et al., 2019), the gastric-type neutral mucin in the cytoplasm of LEGH cells exhibits yellowish, whereas the acidic mucin of EC cells shows pinkish when stained with Papanicolaou staining. This color distinction aids in identifying LEGH cells. However, diagnosing LEGH remains subjective, lacking a quantitative criterion based on mucin color, underscoring the need for objective diagnostic measures.

Quantitative comparisons with MS imaging results and existing methods confirmed the superior performance of our approach in stain quantification. Moreover, the stain unmixing results clearly demonstrated differences in stain abundances between LEGH and EC cells. As an application of our proposed method, we achieved a classification accuracy of 98.0% in differentiating mucin types between LEGH and EC cells based on the quantified stain abundances, surpassing classifications based on color space features.

1.1 Contribution

The contributions of this paper are:

- We propose a novel constraint tailored for Papanicolaou stain, weighted nucleus sparsity, which emphasizes and enhances the sparsity of H in the images. When combined with TV regularization, the approach led to more accurate and biologically consistent stain unmixing.
- We present the first method for unmixing Papanicolaou stain in RGB images. This method provides insights for unmixing RGB images into more than three colors.
- We have preliminarily established quantitative diagnostic criteria to differentiate LEGH from EC cells based on stain unmixing results from RGB images, providing a potential approach for LEGH identification that offers high interpretability for doctors.

The rest of this paper is organized as follows. Section 2 briefly introduces the MS stain unmixing method. Section 3 explains the proposed stain unmixing method for RGB images. Section 4 describes the experiments and results of stain unmixing and classification of EC and LEGH cells. Section 5 discusses the research findings and outlines potential directions for future studies.

2. Multispectral stain unmixing method

In this section, we introduce the method for performing Papanicolaou stain unmixing using MS images proposed in (Takeyama et al., 2025). The stain unmixing results from MS images are considered the ground truth and serve as references

for analyzing the Papanicolaou stain unmixing results from RGB images.

By assuming the Beer-Lambert law, for a certain wavelength λ , the absorbance (i.e., OD) of observation $\alpha(\lambda)$ is modeled by the following formulations:

$$\alpha(\lambda) = \sum_i c_i \varepsilon_i(\lambda), \quad (1)$$

$$I_T(\lambda) = 10^{-\alpha(\lambda)} I_I(\lambda). \quad (2)$$

where c_i is the dye amount and $\varepsilon_i(\lambda)$ is the spectral absorption coefficient of the i -th stain ($i = 1, \dots, R$, and R is the number of dyes). Let $I_I(\lambda)$ and $I_T(\lambda)$ be the intensities of the incident and transmitted light, which are obtained from the glass and stained pixels, respectively. According to Eq. (2), the spectral absorbance $\alpha(\lambda)$ can be calculated by

$$\alpha(\lambda) = \log_{10} \left(\frac{I_I(\lambda)}{I_T(\lambda)} \right). \quad (3)$$

We can define the spectral absorbance of the k -th spectral channel $\alpha(\lambda_k)$ as

$$\alpha(\lambda_k) = \log_{10} \left(\frac{I_I(\lambda_k)}{I_T(\lambda_k)} \right). \quad (4)$$

Then, for each pixel, we get

$$\begin{aligned} \mathbf{y} &= \mathbf{E}\mathbf{x}, \\ \text{s. t. } \mathbf{y} &= [\alpha(\lambda_1), \alpha(\lambda_2), \dots, \alpha(\lambda_M)]^T \in \mathbb{R}^{M \times 1}, \\ \mathbf{E} &= \begin{bmatrix} \varepsilon_1(\lambda_1) & \varepsilon_2(\lambda_1) & \dots & \varepsilon_R(\lambda_1) \\ \varepsilon_1(\lambda_2) & \varepsilon_2(\lambda_2) & \dots & \varepsilon_R(\lambda_2) \\ \vdots & \vdots & \ddots & \vdots \\ \varepsilon_1(\lambda_M) & \varepsilon_2(\lambda_M) & \dots & \varepsilon_R(\lambda_M) \end{bmatrix} \in \mathbb{R}^{M \times R}, \\ \mathbf{x} &= [c_1, c_2, \dots, c_R]^T \in \mathbb{R}^{R \times 1}. \end{aligned} \quad (5)$$

where M is the number of spectral channels. The spectral absorption coefficient matrix \mathbf{E} is normalized such that each column has a unit summation of its elements:

$$\mathbf{1}^T \mathbf{e}_i = 1, \quad (6)$$

where $\mathbf{1}$ is an M -dimensional column vector of ones, and \mathbf{e}_i is the i -th column vector of \mathbf{E} . In (Takeyama et al., 2025), we captured 14-band MS images with spectral information from 440 nm to 720 nm at 20 nm intervals. Since $R < M$ in MS Papanicolaou stain unmixing, we can estimate the stain abundance \mathbf{x} of the pixel by multiplying the pseudoinverse of the spectral absorption coefficient matrix \mathbf{E} with the absorbance vector \mathbf{y} of the captured MS image. The stain absorption matrix \mathbf{E} was computed in advance based on Eq. (4) using MS images of single-stain specimens. For more details on MS stain unmixing, please refer to (Takeyama et al., 2025).

3. Proposed RGB stain unmixing method

In this section, we present the methodology for the proposed stain unmixing algorithm using RGB images.

3.1 Formulation of the RGB stain unmixing problem

Let $\mathbf{I}_1 \in \mathbb{R}^{3 \times n}$ be the matrix of observed RGB intensities in an image, where n is the number of pixels, and let $\mathbf{I}_0 \in \mathbb{R}^{3 \times 1}$ be the RGB (red, green, and blue) intensity of the incident light on the sample (obtained from the glass pixels). For the i -th spectral channel ($i = 1, 2, 3$), the absorbance (i.e., OD) $\mathbf{y}_i \in \mathbb{R}^{1 \times n}$ is

$$\mathbf{y}_i = \log_{10} \frac{\mathbf{l}_i}{I_{0,i}}. \quad (7)$$

where \mathbf{l}_i is the i -th row vector of \mathbf{I}_1 , and $I_{0,i}$ is the i -th element of \mathbf{I}_0 . The influence of the spectral sensitivities of RGB channels is neglected for simplicity.

Stained tissue attenuates light in a certain spectrum depending on the type and amount of dye it has absorbed. Let $\mathbf{A} \in \mathbb{R}^{3 \times r}$ be the stain absorption coefficient matrix (i.e., stain matrix) whose columns represent the absorbance in RGB channels of each dye such that r is the number of dyes, and $\mathbf{X} \in \mathbb{R}^{r \times n}$ be the stain abundance matrix, where the row represents the amount of each dye. Then, we can write

$$\mathbf{Y} = \mathbf{A}\mathbf{X}. \quad (8)$$

When both \mathbf{A} and \mathbf{X} are unknown, it is called a blind unmixing problem, and several methods have been proposed (Gavrilovic et al., 2013; Macenko et al., 2009; Pérez-Bueno et al., 2022; Trahearn et al., 2015; Zheng et al., 2019). Blind unmixing is often employed as an intermediate step in color normalization, where distinct stain matrices are estimated for images exhibiting color variations, and subsequently used in color deconvolution to derive the stain abundance matrix. However, identifying the appropriate stain matrix for Papanicolaou staining in blind unmixing is particularly challenging and often yields multiple valid yet distinct solutions. Incorporating prior knowledge of the spectral absorbance characteristics

of individual dyes can effectively constrain the solution space. In addition, considering practical scenarios, the stain matrix should remain consistent across a set of slides, such as those processed in the same laboratory on the same day or during a certain term, with appropriate quality control of the staining process. In such circumstances, deriving a different stain matrix for each image is unwarranted and may introduce unnecessary variability.

Therefore, we use single-stain RGB images to measure the stain absorption coefficient matrix \mathbf{A} in advance. We excluded BY from the study and considered only the effects of the remaining four dyes (EY, H, LG, and OG) since BY is almost transparent in our case, resulting in $r = 4$. After measuring the stain absorption coefficients of the individual dyes, we perform normalization to ensure that each column vector has a unit summation, ensuring that every dye has a comparable contribution to the calculation

$$\mathbf{1}^T \mathbf{a}_i = 1, \quad (9)$$

where $\mathbf{1}$ is a three-dimensional column vector of ones, and \mathbf{a}_i is the i -th column vector of \mathbf{A} .

As a result, estimating \mathbf{X} becomes a linear inverse problem. However, a challenge arises because the number of dyes in the Papanicolaou stain exceeds the RGB image channels, making the inverse problem, i.e., the unmixing problem, underdetermined. The proposed method employs optimization methods to determine the stain abundance \mathbf{X} .

3.2 Proposed unmixing method based on nonnegativity, weighted nucleus sparsity, and TV regularizations

In optimization, we utilize prior knowledge of stain abundance to design three constraints that limit the solution space. Considering that in Papanicolaou-stained samples the stain abundance cannot be negative, we introduce a nonnegativity regularization. Additionally, we incorporate TV regularization to account for the piecewise smoothness of abundance in the neighboring pixels. Furthermore, H abundance is sparse in the image since H typically binds with the cell nuclei and the cytoplasm is rarely stained by H. We propose a novel regularization, weighted nucleus sparsity regularization to enhance the sparsity of H abundance.

Based on the aforementioned constraints, we formulate the problem of Papanicolaou stain unmixing in RGB images into a regularized linear regression problem. We perform stain unmixing by solving the following optimization problem:

$$\min_{\mathbf{X}} \frac{1}{2} \|\mathbf{A}\mathbf{X} - \mathbf{Y}\|_F^2 + \lambda \|\mathbf{w} \odot \mathbf{x}_H\|_{1,1} + \lambda_{TV} TV(\mathbf{X}) \text{ s.t. } : \mathbf{X} \geq 0, \quad (10)$$

where \odot denotes the elementwise multiplication of two variables, \mathbf{x}_H is a $1 \times n$ row vector representing the abundance of H, and

$$TV(\mathbf{X}) \equiv \sum_{\{i,j\} \in \varepsilon} \|\mathbf{x}_i - \mathbf{x}_j\|_1, \quad (11)$$

is a vector extension of the anisotropic TV (Chambolle, 2004; Rudin et al., 1992), which promotes piecewise constant (or smooth) transitions in the fractional abundance of the same dye among neighboring pixels, ε denotes the set of horizontal and vertical neighbors in the image, and \mathbf{x}_i represents the i -th column of \mathbf{X} .

Let $\mathbf{H}_h: \mathbb{R}^{m \times n} \rightarrow \mathbb{R}^{m \times n}$ denote a linear operator computing the horizontal differences between the components of \mathbf{X} corresponding to neighboring pixels; i.e., $\mathbf{H}_h \mathbf{X} = [\mathbf{d}_1, \mathbf{d}_2, \dots, \mathbf{d}_n]$, where $\mathbf{d}_i = \mathbf{x}_i - \mathbf{x}_{i_h}$ with i and i_h denoting a pixel and its horizontal neighbor. We are assuming periodic boundaries. Let $\mathbf{H}_v: \mathbb{R}^{m \times n} \rightarrow \mathbb{R}^{m \times n}$ be defined in a similar way for the vertical differences; i.e., $\mathbf{H}_v \mathbf{X} = [\mathbf{v}_1, \mathbf{v}_2, \dots, \mathbf{v}_n]$, where $\mathbf{v}_i = \mathbf{x}_i - \mathbf{x}_{i_v}$, with i and i_v denoting a pixel and its vertical neighbor. With these two difference operators, we define

$$\mathbf{H}\mathbf{X} \equiv \begin{bmatrix} \mathbf{H}_h \mathbf{X} \\ \mathbf{H}_v \mathbf{X} \end{bmatrix}. \quad (12)$$

At iteration t , let the stain abundance matrix \mathbf{X}^t consist of four $1 \times n$ row vectors \mathbf{x}_s^t ($s \in \{EY, H, LG, OG\}$), each corresponding to the abundance of one dye (EY, H, LG, and OG).

$$\mathbf{X}^t = \begin{bmatrix} \mathbf{x}_{EY}^t \\ \mathbf{x}_H^t \\ \mathbf{x}_{LG}^t \\ \mathbf{x}_{OG}^t \end{bmatrix}. \quad (13)$$

Let \mathbf{w}^{t+1} be the nucleus sparsity weight vector at iteration $t + 1$ and its i -th element w_i^{t+1} is calculated using the i -th element of H abundance at iteration t , $x_{H,i}^t$:

$$w_i^{t+1} = \exp(-x_{H,i}^t). \quad (14)$$

Then we can use $\mathbf{W} = [\mathbf{0} \ \mathbf{w}^T \ \mathbf{0} \ \mathbf{0}]^T$ to represent the nucleus sparsity weight matrix of the same dimension as \mathbf{X} , obtained by padding the nucleus sparsity weight vector \mathbf{w} with an $n \times 1$ zero-vector $\mathbf{0}$.

With these definitions in place, Prob. (10) can be reformulated as follows:

$$\min_{\mathbf{X}} \frac{1}{2} \|\mathbf{AX} - \mathbf{Y}\|_F^2 + \lambda \|\mathbf{W} \odot \mathbf{X}\|_{1,1} + \lambda_{TV} \|\mathbf{HX}\|_{1,1} + \iota_{R^+}(\mathbf{X}), \quad (15)$$

where $\iota_{R^+}(\mathbf{X}) = \sum_{i=1}^n \iota_{R^+}(\mathbf{x}_i)$ is the indicator function of the nonnegative real number set \mathbb{R}^+ ($\iota_{R^+}(\mathbf{x}_i)$ is zero if \mathbf{x}_i belongs to the nonnegative orthant and $+\infty$ otherwise). At each iteration, \mathbf{W} is updated based on Eq. (14). A lower H abundance in the cytoplasm is assigned a higher constraint weight in the subsequent iteration, effectively reducing the small abundance to zero. Conversely, a larger H abundance in the nucleus receives a lower weight, thus preserving the abundance.

3.3 Algorithm design for the optimization problem

To solve this optimization problem, we construct an algorithm based on the alternating direction method of multipliers (ADMM) (Boyd et al., 2011). In the following text, we explain this algorithm in detail.

Given Prob. (15), we can reformulate it into the following formulation:

$$\begin{aligned} \min_{\mathbf{u}, \mathbf{v}_1, \mathbf{v}_2, \mathbf{v}_3, \mathbf{v}_4, \mathbf{v}_5} & \frac{1}{2} \|\mathbf{V}_1 - \mathbf{Y}\|_F^2 + \lambda \|\mathbf{W} \odot \mathbf{V}_2\|_{1,1} + \lambda_{TV} \|\mathbf{V}_4\|_{1,1} + \iota_{R^+}(\mathbf{V}_5) \\ \text{s. t.} & \mathbf{V}_1 = \mathbf{AX}, \mathbf{V}_2 = \mathbf{X}, \mathbf{V}_3 = \mathbf{X}, \mathbf{V}_4 = \mathbf{HV}_3, \mathbf{V}_5 = \mathbf{X} \end{aligned} \quad (16)$$

By letting

$$\begin{aligned} \mathbf{V} & \equiv (\mathbf{V}_1, \mathbf{V}_2, \mathbf{V}_3, \mathbf{V}_4, \mathbf{V}_5), \\ g(\mathbf{V}) & \equiv \frac{1}{2} \|\mathbf{V}_1 - \mathbf{Y}\|_F^2 + \lambda \|\mathbf{W} \odot \mathbf{V}_2\|_{1,1} + \lambda_{TV} \|\mathbf{V}_4\|_{1,1} + \iota_{R^+}(\mathbf{V}_5) \\ \mathbf{G} & = \begin{bmatrix} \mathbf{A} \\ \mathbf{I} \\ \mathbf{I} \\ \mathbf{0} \\ \mathbf{I} \end{bmatrix}, \quad \mathbf{B} = \begin{bmatrix} -\mathbf{I} & \mathbf{0} & \mathbf{0} & \mathbf{0} & \mathbf{0} \\ \mathbf{0} & -\mathbf{I} & \mathbf{0} & \mathbf{0} & \mathbf{0} \\ \mathbf{0} & \mathbf{0} & -\mathbf{I} & \mathbf{0} & \mathbf{0} \\ \mathbf{0} & \mathbf{0} & \mathbf{H} & -\mathbf{I} & \mathbf{0} \\ \mathbf{0} & \mathbf{0} & \mathbf{0} & \mathbf{0} & -\mathbf{I} \end{bmatrix}, \end{aligned} \quad (17)$$

Prob. (16) is reduced as follows:

$$\min_{\mathbf{U}, \mathbf{V}} g(\mathbf{V}) \text{ s. t. } \mathbf{GX} + \mathbf{BV} = \mathbf{0}. \quad (18)$$

The pseudocode solving Prob. (18) is shown in Algorithm 1, where

$$L(\mathbf{X}, \mathbf{V}, \mathbf{D}) \equiv g(\mathbf{V}) + \frac{\mu}{2} \|\mathbf{GX} + \mathbf{BV} - \mathbf{D}\|_F^2, \quad (19)$$

is the augmented Lagrangian for Prob. (16). The constant μ is positive, and \mathbf{D} denotes the Lagrange multipliers associated with the constraint $\mathbf{GX} + \mathbf{BV} = \mathbf{0}$. We also present in Appendix A the details of the optimization with respect to \mathbf{X} and \mathbf{V} of the ADMM Algorithm 1. The implementation of the proposed method is publicly available¹.

Algorithm 1: Pseudocode for solving Prob. (16).

1: **Initialization:**

set $k = 0$, choose $\mu > 0$, $\mathbf{X}^{(0)}$, $\mathbf{V}^{(0)}$, $\mathbf{D}^{(0)}$

2: **repeat:**

$$3: \mathbf{W}^{(k+1)} = \begin{bmatrix} \mathbf{0} \\ \exp(-\mathbf{X}^{(k)}(2, :)) \\ \mathbf{0} \\ \mathbf{0} \end{bmatrix}$$

$$4: \mathbf{X}^{(k+1)} \leftarrow \operatorname{argmin}_{\mathbf{X}} L(\mathbf{X}, \mathbf{V}^{(k)}, \mathbf{D}^{(k)})$$

$$5: \mathbf{V}^{(k+1)} \leftarrow \operatorname{argmin}_{\mathbf{V}} L(\mathbf{X}^{(k+1)}, \mathbf{V}, \mathbf{D}^{(k)})$$

$$6: \mathbf{D}^{(k+1)} \leftarrow \mathbf{D}^{(k)} - \mathbf{GX}^{(k+1)} - \mathbf{BV}^{(k+1)}$$

$$7: \text{Update iteration: } k \leftarrow k + 1$$

$$8: \text{until some stopping criterion is satisfied.}$$

3.4 Abundance normalization by reference values

When presenting quantitative results, normalizing the estimated stain abundance to the range $[0, 1]$ makes it easier to observe and interpret. To achieve this, we determined the reference values for each dye by selecting well-stained areas from the Papanicolaou stain images. Then, we considered the robust maximum value of stain abundance (e.g., the top 1% value)

¹ <https://github.com/ChrisG0ng/SUnWNS-TV>.

as the reference value q_i ($i = 1,2,3,4$). The normalized stain abundance was obtained by dividing the actual stain abundance by this reference value.

4. Experiments and results

This section begins by describing the preparation of Papanicolaou-stained and single-stain slides. We then explain how the RGB images for unmixing were obtained. Then, the estimation of the stain absorption coefficient matrix is demonstrated. The proposed method was evaluated using RGB images converted from MS data, with the unmixing results from MS stain unmixing serving as the ground truth. To quantitatively evaluate our proposed RGB stain unmixing, we calculated the calibration coefficients between MS and RGB stain unmixing results using single-stain images. Additionally, we assessed the performance of our method in terms of stain quantification and cell sample classification.

4.1 Specimen preparation

Six Papanicolaou-stained uterine cervix specimens were collected from six patients, including three EC cases and three LEGH cases. The staining was performed using Carrazzi's hematoxylin solution (Hematoxylin, Sigma-Aldrich, STL, MO, USA), OG-6 (Muto Pure Chemicals Co., Ltd.), and EA-50 (Muto Pure Chemicals Co., Ltd.). For the single-stain procedure, LG, EY, and BY were employed to replicate the composition found in EA-50, creating individual stain solutions. These solutions were then used to stain the collected uterine cervix specimens, producing single-stain results. The staining times were set as follows: 85 seconds for Carrazzi's hematoxylin, 65 seconds for OG-6, and 170 seconds for each dye within EA-50 (LG, EY, BY). For each dye, three single-stain uterine cervix specimens were prepared. All specimens were prepared simultaneously using standardized protocols and stored under identical environmental conditions to minimize potential color variations arising from differences in staining procedures or storage environments.

4.2 RGB image acquisition

In the experiments, we employed the MS microscopic camera (Vectra[®]3, PerkinElmer Inc.) to capture the spectral information of specimens. Samples were captured at 40 \times magnification across 14 spectral bands ranging from 440 nm to 720 nm, with 20 nm intervals between bands. The resulting images had a resolution of 1020 \times 1368 pixels. For subsequent experimental analysis, we converted MS images into RGB images. Since we aim to perform pixel-level comparisons between stain unmixing results from RGB and MS images, generating RGB images from MS data minimizes discrepancies arising from differences in imaging systems—such as spatial resolution, focus areas, depth of field, and image misalignment—ensuring that performance evaluation metrics reflect only the effects of the stain unmixing methods themselves.

To generate RGB images from spectral data of MS images, we first converted the spectral data into CIE XYZ values. Since Papanicolaou staining is a transmissive case, we must consider the reference illuminant. Here we used CIE standard illuminant D65 as the reference illuminant. Thus, the normalized XYZ values were calculated using the following formula:

$$\begin{aligned} X &= \frac{1}{N} \sum_k \bar{x}_k S_k I_k \Delta\lambda, \\ Y &= \frac{1}{N} \sum_k \bar{y}_k S_k I_k \Delta\lambda, \\ Z &= \frac{1}{N} \sum_k \bar{z}_k S_k I_k \Delta\lambda, \\ N &= \sum_k \bar{y}_k I_k \Delta\lambda. \end{aligned} \quad (20)$$

where \bar{x}_k , \bar{y}_k , and \bar{z}_k are the CIE XYZ color matching functions, S_k is the spectral transmittance of the sample in the k -th spectral channel, I_k is the spectral power distribution of the reference illuminant D65 in the k -th spectral channel.

Then, given an XYZ color whose components were in the nominal range $[0, 1]$ and whose reference white was the same as that of the RGB system, the conversion to standard RGB (sRGB) was done in two steps.

Firstly, linear RGB, $[rgb]$, was calculated by

$$\begin{bmatrix} r \\ g \\ b \end{bmatrix} = M^{-1} \begin{bmatrix} X \\ Y \\ Z \end{bmatrix}, \quad (21)$$

where M is the 3×3 RGB-to-XYZ transformation matrix. Then, the linear RGB channels $o \in \{r, g, b\}$ were transformed into $O \in \{R, G, B\}$ through gamma correction to generate sRGB images.

$$O = \begin{cases} 12.92o & \text{if } o \leq 0.0031308 \\ 1.055o^{\frac{1}{2.4}} - 0.055 & \text{otherwise} \end{cases} \quad (22)$$

As a result, we initially captured MS images from single-stain specimens for each dye. Corresponding sRGB images were generated from these MS images (Table 1) to facilitate the measurement of stain matrix (see Section 4.3). Subsequently, we acquired MS images from several Papanicolaou-stained specimens and converted them into sRGB images. Table 2 summarizes the number of images containing EC and LEGH cells captured from each Papanicolaou-stained slide. These images were utilized to evaluate the quantification performance of the proposed RGB stain unmixing method (see Section 4.5). However, for assessing cell classification based on the unmixing results (see Section 4.7), only images from slides 1 to 5 were employed to avoid potential annotation errors.

Table 1. The number of single-stain images.

	EY	H	LG	OG	BY
Number	18	21	17	19	18

Table 2. The number of Papanicolaou-stained images.

Slide No. (Annotation)	Slide 1 (EC)	Slide 2 (EC)	Slide 3 (EC)	Slide 4 (LEGH)	Slide 5 (LEGH)	Slide 6 (LEGH)
Image of EC cells	7	10	11	0	0	11
Image of LEGH cells	0	0	0	10	14	12
Image of both EC & LEGH cells	0	0	0	0	0	4

Figure 1 shows the sRGB image converted from the MS image and the RGB image cropped from the same sample region in the WSI. All WSIs were acquired using a WSI scanner (NanoZoomer2.0-HT, Hamamatsu Photonics Corp.) at 40 \times magnification. The color reproduction in this manner was not completely equivalent but acceptable, since accurate color reproduction was not the objective of this study. For simplicity, we use the term “RGB image” to refer to the sRGB image that has been converted from an MS image in the subsequent text of this paper, unless otherwise specified.

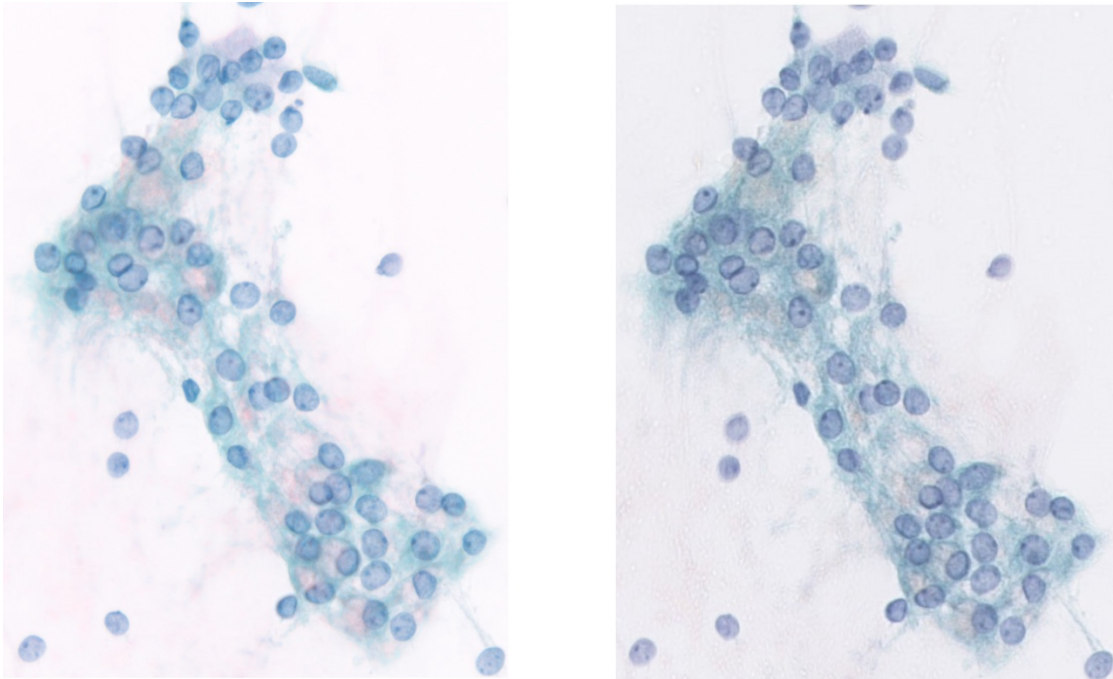


Figure 1. RGB image converted from the MS image (left), and RGB image cropped from the WSI (right).

4.3 Measurement of stain absorption coefficient matrix

We used single-stain images to determine the stain absorption coefficient matrices required for unmixing. Some captured images are displayed in Figure 2. The lipid stained with BY was hard to observe, and lipid detection was less crucial in the observation of mucinous cytoplasm. Thus, we considered only EY, H, LG, and OG dyes in our study. As illustrated by the blue-shaded areas in Figure 2, we cropped eight well-stained samples from the single-stain images for each dye, then calculated, averaged, and normalized their absorbances to get the absorption coefficients.

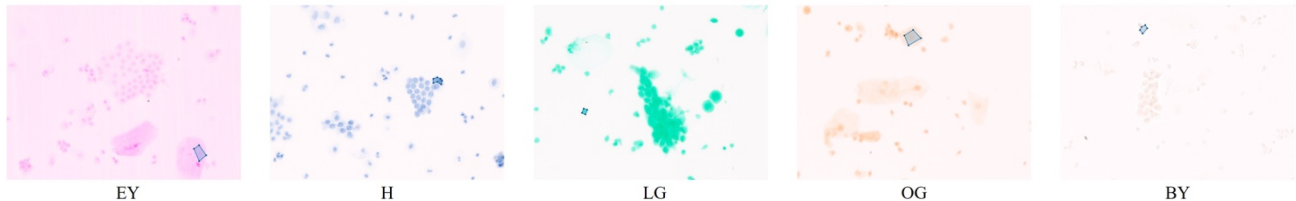


Figure 2. Examples of single-stain images used to calculate the stain absorption coefficients.

Figure 3 illustrates the 14-band MS and RGB absorption coefficients of EY, H, LG, and OG. It can be observed that the conventional H and EY exhibit some spectral overlap within their primary absorption bands; however, the overall spectral differentiation remains relatively clear. With the inclusion of LG and OG, the spectral overlap among the dyes becomes more intricate. For instance, significant overlap between OG and EY occurs in the 500–530 nm range, while notable intersections between H and LG are found within the 600–660 nm range, and between H and OG around 520 nm. These overlaps impose greater challenges on color unmixing algorithms, necessitating additional constraints to achieve accurate stain unmixing.

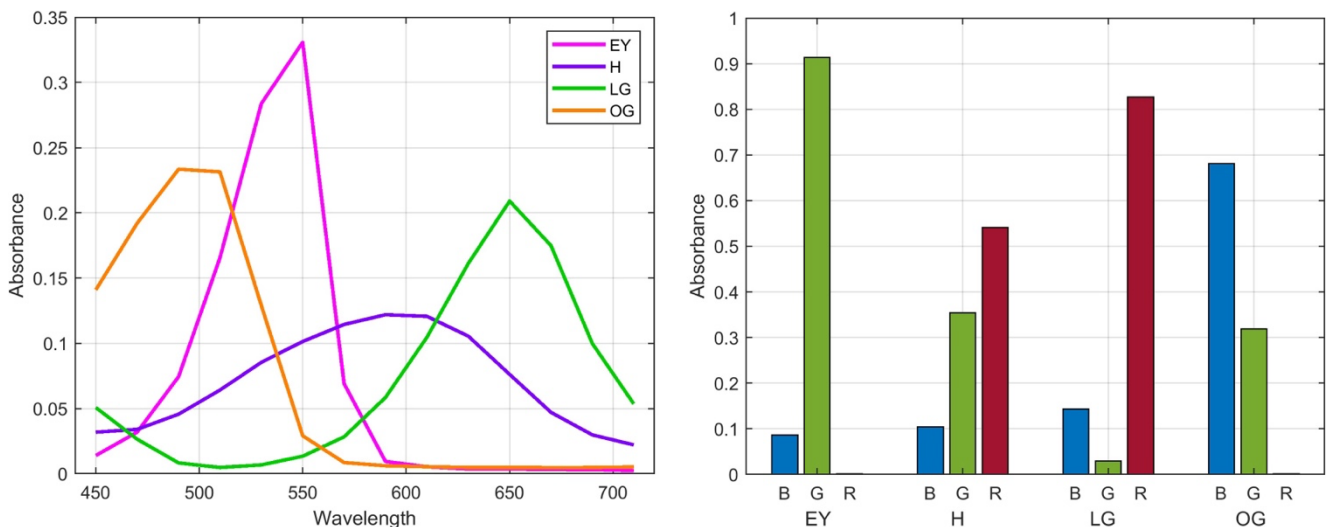


Figure 3. MS absorption coefficients (left), and RGB absorption coefficients (right) of Papanicolaou stain.

4.4 Abundance calibration between MS and RGB stain unmixing

The results of MS stain unmixing were considered the ground truth and served as references for analyzing the results of RGB stain unmixing. To enable the quantitative comparison, we calculated the calibration coefficient, which is the ratio of the stain abundances obtained by MS stain unmixing to those obtained by RGB stain unmixing. We calculated a calibration coefficient for each dye.

For instance, with the i -th dye ($i = 1, 2, 3, 4$), we began by selecting a typical single-stain sample and calculating its MS absorbance $\mathbf{Y}_i \in \mathbb{R}^{14 \times m}$ and RGB absorbance $\mathbf{Y}'_i \in \mathbb{R}^{3 \times m}$, where m is the number of pixels in the sample. Here, we assume the presence of only that dye in the sample, so we have

$$\mathbf{e}_i \mathbf{s}_i = \mathbf{Y}_i, \quad (23)$$

$$\mathbf{a}_i \mathbf{s}'_i = \mathbf{Y}'_i, \quad (24)$$

where $\mathbf{e}_i \in \mathbb{R}^{14 \times 1}$ is the MS absorption coefficient vector of the i -th dye, $\mathbf{a}_i \in \mathbb{R}^{3 \times 1}$ is the RGB absorption coefficient vector of this dye, $\mathbf{s}_i \in \mathbb{R}^m$ and $\mathbf{s}'_i \in \mathbb{R}^m$ denote the MS and RGB stain abundance vector of the single-stain sample, respectively.

\mathbf{s}_i and \mathbf{s}'_i were computed using the least squares method.

Subsequently, we used least squares to calculate the calibration coefficient p_i :

$$p_i = \arg \min_{p_i} \sum_{j=1}^m (p_i \mathbf{s}'_{ij} - \mathbf{s}_{ij})^2 = \frac{\mathbf{s}'_i \cdot \mathbf{s}_i}{\mathbf{s}'_i \cdot \mathbf{s}'_i}. \quad (25)$$

The calibration coefficients between the stain abundances obtained by MS stain unmixing and those obtained by RGB stain unmixing were $p_1 = 7.51, p_2 = 13.13, p_3 = 12.36, p_4 = 5.79$. It is important to note that this calibration was intended solely to facilitate numerical comparisons with MS stain unmixing results; it is not a necessary step for performing RGB stain unmixing itself.

4.5 Evaluation of stain quantification performance

We evaluated the proposed RGB stain unmixing algorithm using the generated RGB images of the Papanicolaou-stained specimens. As described in Section 3.4, we normalized all stain abundances within the range $[0, 1]$. The reference values for normalizing stain abundance were determined as $q_1 = 3.20, q_2 = 6.87, q_3 = 5.78, q_4 = 2.97$.

For quantitative analysis, the MS stain unmixing results were considered the ground truth. To evaluate the unmixing accuracy, we employed two widely recognized metrics: Signal-to-Reconstruction Error (SRE), measured in decibels (dB), and Root Mean Square Error (RMSE). SRE assesses the fidelity of the reconstructed signal relative to the original, with higher values indicating better reconstruction quality. RMSE quantifies the average magnitude of the error between the estimated and true values, where lower values signify more accurate estimations.

$$\text{SRE}(\text{dB}) = 10 \log_{10} (E(\|\mathbf{X}_{GT}\|_F^2) / E(\|\mathbf{X}_{GT} - \hat{\mathbf{X}}\|_F^2)), \quad (26)$$

$$\text{RMSE} = \sqrt{\|\mathbf{X}_{GT} - \hat{\mathbf{X}}\|_F^2 / n}, \quad (27)$$

where $\hat{\mathbf{X}}$ is the abundance estimated by the RGB stain unmixing method, \mathbf{X}_{GT} is the ground truth, $E(\cdot)$ denotes the expectation function, and n is the total number of elements in the matrix (i.e., rows \times columns \times bands).

For the comparative analysis with the quantification results of our proposed method, we also report the results of CD (Ruifrok et al., 2001), SNMF (Vahadane et al., 2016), and SUnSAL-TV (Iordache et al., 2012). To the best of our knowledge, no standardized benchmark or widely accepted unmixing algorithm exists for Papanicolaou-stained images. Consequently, these methods were adapted for application to Papanicolaou stain unmixing. CD was originally developed for H&E staining, so we adapted it for Papanicolaou stain by computing the Moore–Penrose pseudoinverse of the stain matrix as the color deconvolution matrix. SNMF, being a blind stain separation technique that jointly estimates both the stain matrix and stain abundance matrix, was modified to estimate only the stain abundances using the fixed stain matrix to ensure a fair comparison. Although SUnSAL-TV was originally developed for spectral unmixing in remote sensing, its applicability to biomedical imaging has been previously explored (Rossetti et al., 2020).

First, we randomly selected six images from different slides for performance evaluation and optimal parameter estimation: two images containing EC cells, two with LEGH cells, and two containing both EC and LEGH cells, as illustrated in Figure 4. Table 3 summarizes the stain unmixing performance of CD, SNMF, SUnSAL-TV, and the proposed method across these images. For the SNMF, SUnSAL-TV, and our proposed method, only the best results are reported, along with the regularization parameters used. We then computed the root mean square of six parameter sets to determine the tuned parameters and for SNMF ($\lambda = 3 \times 10^{-3}$), SUnSAL-TV ($\lambda = 2 \times 10^{-4}, \lambda_{TV} = 2 \times 10^{-2}$), and the proposed method ($\lambda = 2 \times 10^{-6}, \lambda_{TV} = 1 \times 10^{-3}$). The rightmost column of Table 3 presents the results of the proposed method using its tuned parameter set. Table 3 clearly demonstrates that the proposed method achieved the best stain unmixing results for every individual sample, highlighting its accuracy for unmixing Papanicolaou-stained samples. In terms of overall performance across the six images, the methods can be ranked as follows: Ours $>$ SUnSAL-TV $>$ SNMF $>$ CD. Besides, the optimal parameter values for the proposed method are relatively consistent across different images, suggesting that a parameter set optimized for one image tends to perform well on others. The results of the proposed method using the fixed tuned parameters demonstrate its robustness to images and cell types. In contrast, the optimal parameter sets for SUnSAL-TV vary significantly from image to image, indicating that a parameter set effective for one image may not yield good results for others.

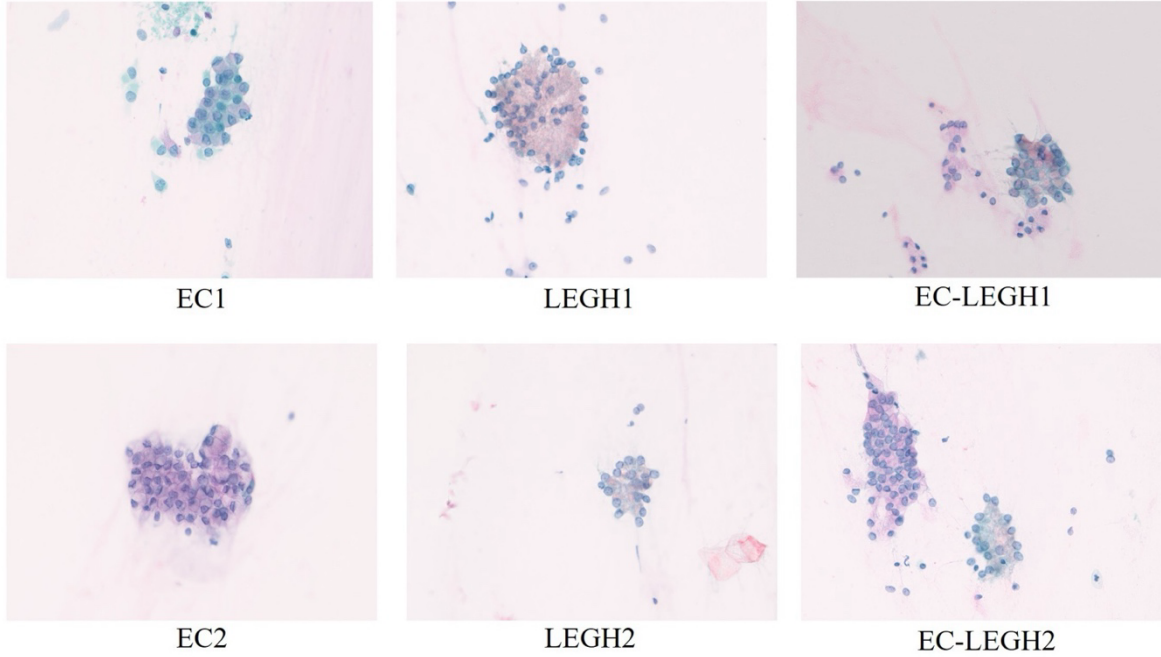


Figure 4. RGB images of cell samples. EC: (a)(d), LEGH: (b)(e), mixed EC-LEGH: (c)(f).

Table 3. Stain unmixing results evaluated by SRE and RMSE.

Image	CD ^a		SNMF ^b		SUnSAL-TV		Ours		Ours (using tuned paras)	
EC1	9.66	0.050	11.09	0.043	11.67	0.040	14.34	0.029	14.33	0.029
	/		$\lambda=4e-3$		$\lambda=3e-4, \lambda_{TV}=4e-2$		$\lambda=2e-6, \lambda_{TV}=9e-4$		$\lambda=2e-6, \lambda_{TV}=1e-3$	
EC2	9.64	0.074	9.93	0.072	10.15	0.070	14.43	0.043	14.41	0.043
	/		$\lambda=4e-3$		$\lambda=5e-4, \lambda_{TV}=2e-2$		$\lambda=2e-6, \lambda_{TV}=7e-4$		$\lambda=2e-6, \lambda_{TV}=1e-3$	
LEGH1	9.12	0.066	9.37	0.064	9.93	0.060	12.77	0.043	12.75	0.043
	/		$\lambda=4e-3$		$\lambda=1e-6, \lambda_{TV}=3e-4$		$\lambda=3e-6, \lambda_{TV}=2e-3$		$\lambda=2e-6, \lambda_{TV}=1e-3$	
LEGH2	10.15	0.041	10.31	0.040	10.68	0.039	13.19	0.029	12.61	0.031
	/		$\lambda=4e-3$		$\lambda=9e-7, \lambda_{TV}=2e-4$		$\lambda=1e-6, \lambda_{TV}=6e-4$		$\lambda=2e-6, \lambda_{TV}=1e-3$	
EC-LEGH1	10.11	0.044	9.83	0.045	11.32	0.038	13.50	0.030	13.50	0.030
	/		$\lambda=2e-3$		$\lambda=1e-6, \lambda_{TV}=1e-2$		$\lambda=2e-6, \lambda_{TV}=1e-3$		$\lambda=2e-6, \lambda_{TV}=1e-3$	
EC-LEGH2	11.08	0.030	10.91	0.031	12.00	0.027	13.37	0.023	11.94	0.027
	/		$\lambda=2e-3$		$\lambda=6e-8, \lambda_{TV}=5e-3$		$\lambda=1e-6, \lambda_{TV}=1e-3$		$\lambda=2e-6, \lambda_{TV}=1e-3$	

^a Used the Moore–Penrose pseudoinverse of the stain matrix as the color deconvolution matrix.

^b Fixed the stain matrix and estimated only the stain abundances.

Figure 5 and Figure 6 present the ground truth of stain abundances, the estimated stain abundance maps, and corresponding difference maps for EY, H, LG, and OG obtained using CD, SNMF, SUnSAL-TV, and the proposed method. Figure 5 shows the results for the image EC1, while Figure 6 shows those for the image LEGH1. In each row, the upper panels display the estimated stain abundance maps, and the lower panels show the pixel-wise differences from the ground truth. For each abundance map, two evaluation metrics—SRE and RMSE—are reported at the bottom left and bottom right corners, respectively. Qualitatively, all four dyes are visibly present in both the EC and LEGH samples. It becomes evident that the conventional sparsity term, assuming dyes are sparse (i.e., only a small number of dyes exist simultaneously) in the image, is not suitable for Papanicolaou-stained images. Compared to the EC sample, the LEGH sample exhibits differences in stain abundance, such as OG showing higher intensity. The difference maps further reveal that the proposed method produces the smallest deviations from the ground truth among all methods, particularly in the cytoplasmic regions. This suggests that the proposed weighted nucleus sparsity constraint effectively mitigates the overestimation of H in non-nuclear regions, thereby improving the estimation accuracy for all four dyes. Quantitatively, the proposed method achieves higher SRE and lower RMSE values across most dyes, indicating superior unmixing performance.

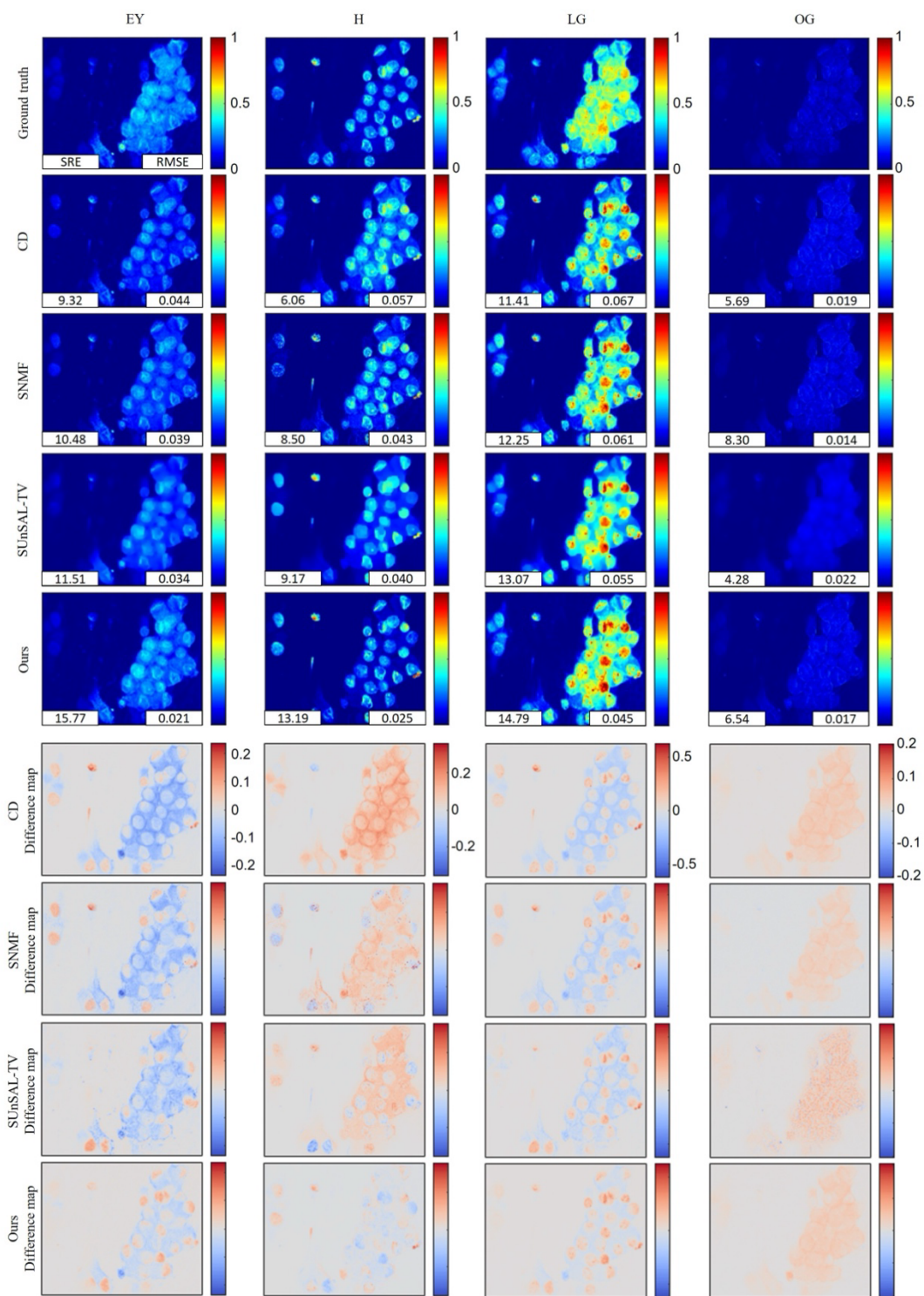


Figure 5. Estimated stain abundance maps and corresponding difference maps compared to ground truth for CD, SNMF, SUnSAL-TV, and the proposed method, applied to a Papanicolaou-stained EC cell sample (Figure 4 EC1). Each abundance map includes two evaluation metrics: SRE (bottom left) and RMSE (bottom right), both computed separately for each dye.

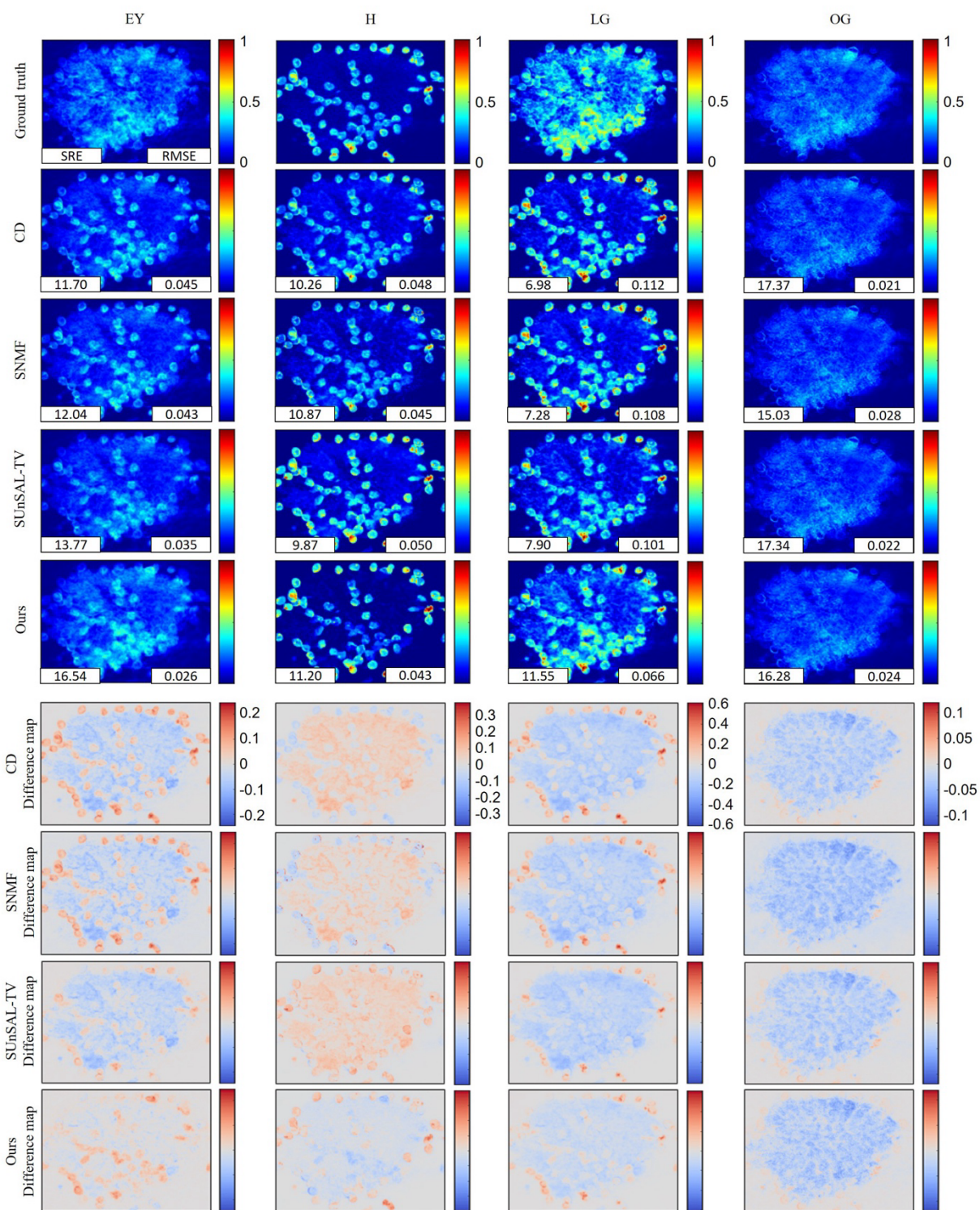


Figure 6. Estimated stain abundance maps and corresponding difference maps compared to ground truth for CD, SNMF, SUnSAL-TV, and the proposed method, applied to a Papanicolaou-stained LEGH cell sample (Figure 4 LEGH1). Each abundance map includes two evaluation metrics: SRE (bottom left) and RMSE (bottom right), both computed separately for each dye.

Then, we applied these methods to the rest of the test images using the tuned parameter sets. Figure 7 and Figure 8 quantitatively compares the unmixing performance of CD, SNMF, SUnSAL-TV, and the proposed method across the remaining test images based on SRE and RMSE. In Figure 7, which summarizes the overall performance across all dyes, our method achieved the highest mean SRE (12.67 dB) and the lowest mean RMSE (0.023), outperforming CD (10.17 dB and 0.031), SNMF (10.27 dB and 0.030), and SUnSAL-TV (11.00 dB and 0.028). This indicates superior quantification fidelity and lower estimation error of the proposed method. To further analyze the performance at the individual dye level, we show the violin plots of SRE and RMSE for each dye (EY, H, LG, OG) in Figure 8. The proposed method consistently yielded higher SRE and lower RMSE across most dye components, especially in EY and LG, suggesting enhanced unmixing accuracy even under complex multi-stain conditions. Notably, the RMSE distributions in both figures show that our method significantly reduces the occurrence of high-error cases, indicating improved robustness in stain unmixing.

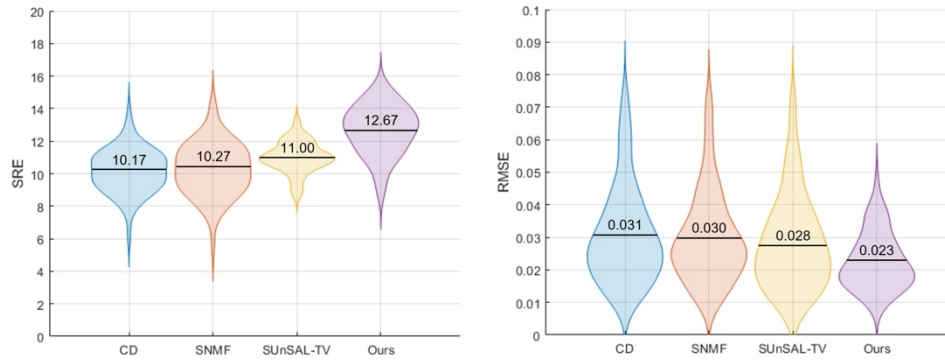


Figure 7. Violin plots of overall SRE (left) and RMSE (right) achieved by CD, SNMF, SUnSAL-TV, and the proposed method on the test images. The black horizontal bars indicate the mean values.

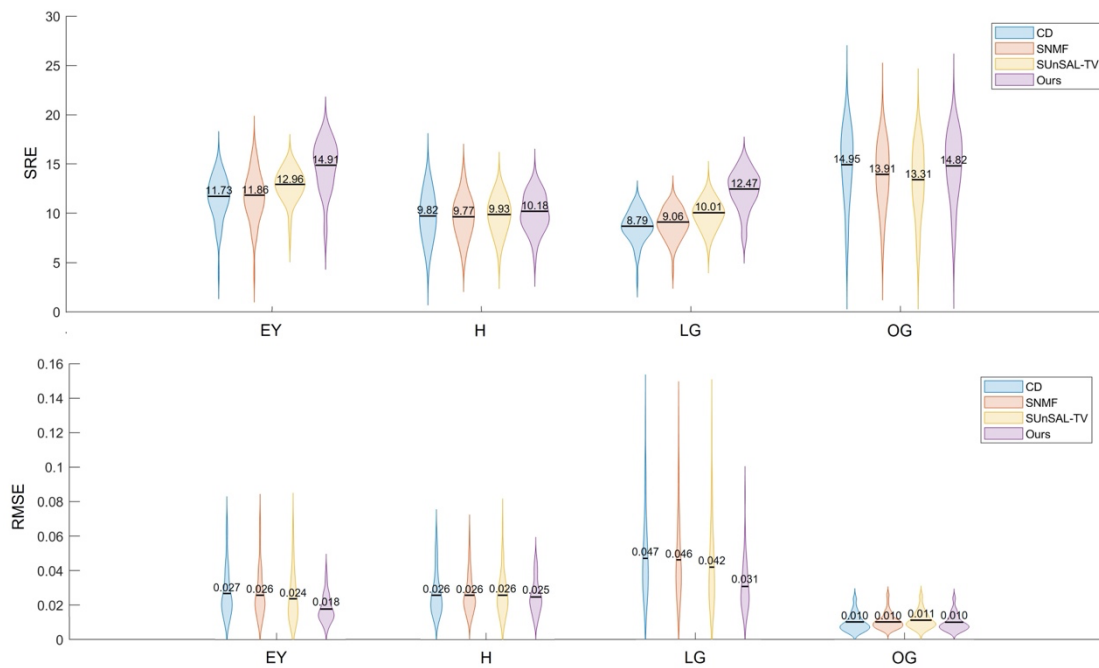


Figure 8. Violin plots of SRE (top) and RMSE (bottom) for each dye (EY, H, LG, OG) obtained by CD, SNMF, SUnSAL-TV, and the proposed method on the test images. The black horizontal bars indicate the mean values.

4.6 Parameter sensitivity

In this section, we analyzed the impact of the regularization parameters involved in the considered methods. Figure 9, using SNMF, SUnSAL-TV, and the proposed method as examples, illustrates the relationship between the SRE values obtained on a mixed EC-LEGH sample (Figure 4 EC-LEGH1) and the parameters (λ and λ_{TV}). From Figure 9, it can be observed that the proposed method achieves higher SRE values than the optimal results of the comparative methods over a wide range of parameters, making it easier to attain better unmixing results. Notably, the performance of the proposed method does not peak when any parameter approaches zero, suggesting that removing the corresponding regularization reduces effectiveness. Optimal performance is observed when λ and λ_{TV} approach 2×10^{-6} and 1×10^{-3} , respectively. This suggests that the combined effect of weighted nucleus sparsity and TV regularization is crucial. In contrast, the l1 sparsity regularization in the comparative methods shows no significant improvement in SRE values across its parameter range, highlighting its ineffectiveness in Papanicolaou stain unmixing.

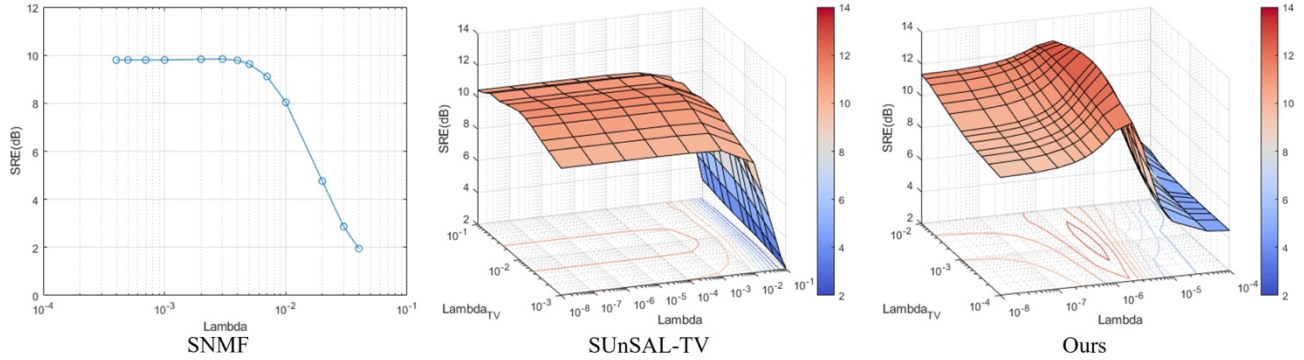


Figure 9. SRE as a function of regularization parameters for an EC-LEGH sample (Figure 4 EC-LEGH1): λ for SNMF (left), λ and λ_{TV} for SUnSAL-TV (middle), and for the proposed method (right).

4.7 Cell classification based on stain unmixing

To quantitatively analyze the differences in stain abundance between EC and LEGH cells, we extracted 248 EC mucin patches and 256 LEGH mucin patches, each measuring 5×5 pixels (Figure 10), from the cytoplasmic regions of Papanicolaou-stained images corresponding to EC and LEGH cases, respectively. Then, we calculated the average stain abundance \bar{x} for each patch. Given that the stain abundance \bar{x} may correlate with the concentration and thickness of mucin in the cytoplasm, it is appropriate to compare the relative stain abundance $\bar{x}_{\text{relative}}$, which is invariant to the thickness. It is calculated as follows:

$$\bar{x}_{\text{relative},i} = \frac{\bar{x}_i}{\sum_{i=1}^4 \bar{x}_i}. \quad (28)$$

where \bar{x}_i and $\bar{x}_{\text{relative},i}$ are the average stain abundance and relative stain abundance of the i -th dye, respectively.

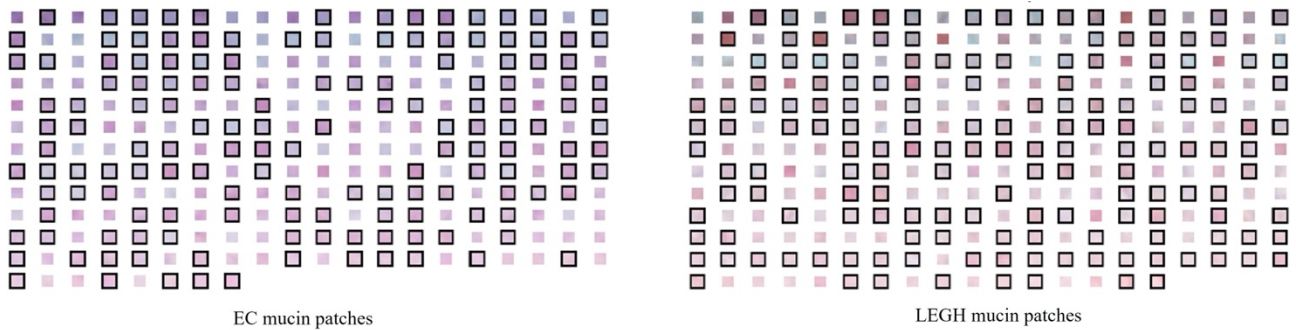


Figure 10. Patches of EC and LEGH mucin (patches in black boxes are the training data, and the rest are the test data).

The Mann-Whitney U-test, a nonparametric test, was used to determine if there were significant differences in relative stain abundance between LEGH and EC cells. The MS stain unmixing results were considered the ground truth. Figure 11

presents box plots of the relative stain abundance for each dye derived from (a) MS stain unmixing and (b) the proposed RGB stain unmixing method, along with their p-values.

According to the results of the proposed method, significant differences are observed in EY, LG, and OG relative abundances ($p < 0.001$). In the MS results, significant differences exist in the relative abundances of EY, H, and OG ($p < 0.001$). The discrepancies between methods reside in the H and LG channels. The larger p-value for H produced by the proposed method is attributable to the spectral limitations of RGB images. The significant LG difference detected by the RGB-based method—but not by the MS analysis—may stem from the RGB model’s assumption of a linear relationship between stain abundance and RGB absorbance. Despite these discrepancies, both subfigures consistently show that LEGH samples have a noticeably lower relative abundance of EY and a higher abundance of OG compared to EC samples. Therefore, the relative stain abundances of EY and OG obtained through stain unmixing can be effectively used to distinguish between EC and LEGH cell mucin.

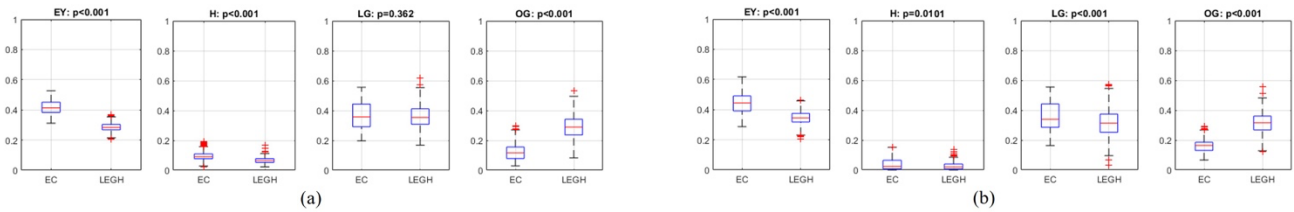


Figure 11. Box plot of the relative stain abundance of each dye with each p-value using the Mann-Whitney U-test: (a) MS stain unmixing, and (b) the proposed RGB stain unmixing method.

To further assess the utility of stain abundance quantification in cytological diagnosis, we employed relative stain abundances derived from our proposed unmixing method to classify mucin in EC and LEGH cells. To maintain high interpretability in the classification process, we selected linear discriminant analysis (LDA) as our classifier. For comparative analysis, we also trained LDA models using RGB intensities, OD values, CIELAB values, and relative stain abundances obtained from MS unmixing, respectively. The following feature sets were used to train the LDA classifiers:

- RGB intensities: The model used the raw red, green, and blue channel intensities as input features.
- OD values: The model used the OD values computed from the red, green, and blue channels.
- CIELAB values: The model used the L^* , a^* , and b^* components of the CIELAB color space.
- MS-based stain abundances: The model used the relative stain abundances (EY, H, and OG) obtained from MS stain unmixing.
- Proposed RGB-based stain abundances: The model used the relative stain abundances of EY and OG derived from the proposed RGB stain unmixing method.

From the patches illustrated in Figure 10, we randomly selected 148 EC and 156 LEGH mucin patches as the training set, with the remaining 100 EC and 100 LEGH patches reserved for testing. The resulting LDA score density and classification plots for each LDA model are shown in Figure 12, where EC patches are marked with circles, LEGH patches with squares, and misclassified patches with crosses. The decision boundary is depicted either by a black line or a yellow plane. Gray-shaded areas in the LDA score density plots indicate where misclassification occurred.

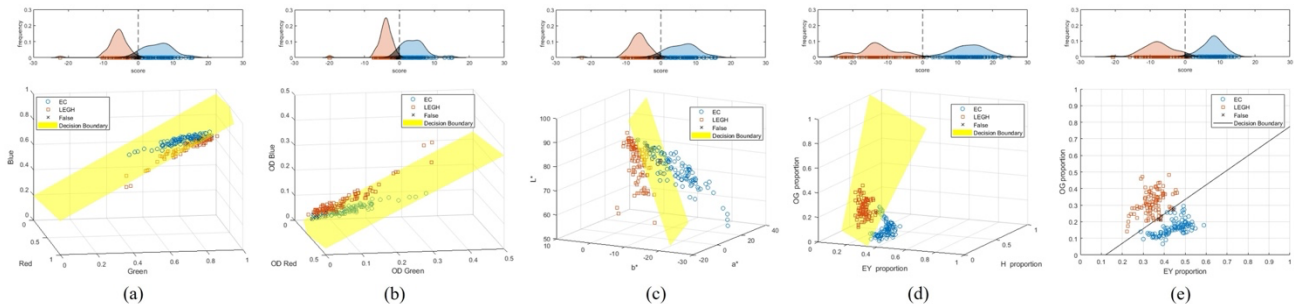


Figure 12. LDA score density plots (top row) and corresponding classification results (bottom row) using different feature sets: (a) RGB intensities, (b) OD values, (c) CIELAB values, (d) relative stain abundances from MS unmixing, and (e) relative stain abundances from the proposed RGB unmixing method.

Table 4 presents the four key quality metrics of the classification results—accuracy, precision, recall, and F1 score—which together provide a comprehensive evaluation of each LDA model’s performance. The linear discriminant function $D(\mathbf{x})$ of the proposed classification method was derived as follows:

$$D(\mathbf{x}) = 57.96EY - 65.84OG - 6.99. \quad (29)$$

The patch was classified into LEGH if $D(\mathbf{x}) \geq 0$ and EC if $D(\mathbf{x}) < 0$.

Table 4. Four quality measures of LDA models.

LDA model	Accuracy	Precision	Recall	F1 score
RGB intensity	0.965	0.943	0.990	0.966
OD	0.945	0.908	0.990	0.947
CIELAB value	0.950	0.925	0.980	0.952
Relative stain abundances from MS unmixing	0.995	1.000	0.990	0.995
Relative stain abundances from the proposed RGB unmixing	0.980	1.000	0.960	0.980

The numerical results indicate that the LDA classifier based on the proposed RGB unmixing method achieved outcomes closest to those based on MS stain unmixing results, outperforming classifiers based on RGB intensity, OD, and CIELAB value. As illustrated by Figure 10, it is difficult to visually distinguish between EC and LEGH cells based on color differences. The separations of EC and LEGH patches based on RGB intensity, OD, and CIELAB value show less clarity, as reflected by larger overlapping areas in the LDA score density plots. However, the distinction between EC and LEGH patches is more pronounced when using relative stain abundances derived from MS or RGB stain unmixing. The 2D classification plot reveals that the yellow hue of LEGH mucin corresponds to a higher relative abundance of OG and a lower relative abundance of EY. These results indicate that the proposed RGB stain unmixing method can effectively quantify dye amounts and that employing relative stain abundances as features enhances both the accuracy and explainability of distinguishing EC from LEGH samples.

5. Discussion and Conclusions

To date, limited research has specifically addressed stain unmixing in Papanicolaou-stained images. This paper introduces the first stain unmixing method for RGB images of Papanicolaou-stained specimens. Utilizing the prior knowledge that H typically concentrates in the nuclei rather than the cytoplasm, we propose a novel constraint term, weighted nucleus sparsity regularization. This term is combined with nonnegativity and TV regularization to estimate effectively the stain abundances for four dyes (EY, H, LG, and OG) from three-channel RGB images by solving an optimization problem. Through both qualitative and quantitative experiments, the proposed method demonstrated superior performance across multiple evaluation metrics when compared to three baseline techniques: CD, SNMF, and SUnSAL-TV. These findings not only validate the effectiveness of the proposed method for Papanicolaou stain unmixing but also provide a methodological foundation for future work on stain unmixing in scenarios where the number of dyes exceeds the number of image channels.

In our experiments, the stain matrix was predetermined using single-stain slides, and the stain unmixing results from MS images were regarded as the ground truth, as established in (Takeyama et al., 2025). The quantitative results (Sections 4.5–4.6) indicate that the proposed method consistently achieved higher SRE and lower RMSE values across six representative images. Notably, this performance was maintained even when employing a single set of fixed regularization parameters, demonstrating robustness to sample variability and minimal dependence on parameter fine-tuning. The visualizations of the estimated stain abundance maps and difference maps further corroborate the method’s stability across different cell types, particularly in cytoplasmic regions where overestimation of H is commonly observed. These findings underscore the effectiveness of integrating the weighted nucleus sparsity constraint with TV regularization in addressing the challenges posed by overlapping spectral absorbance among multiple dyes. Performance comparisons using violin plots confirmed the proposed method’s advantage in both overall and per-dye unmixing accuracy. The narrow RMSE distributions and fewer high-error outliers observed for the proposed method indicate improved consistency and robustness under multi-dye staining conditions. Additionally, the parameter sensitivity analysis revealed that the proposed method outperforms comparative approaches over a broad parameter range, further reinforcing its practical usability.

The quantitative results also demonstrated the utility of the proposed method in downstream diagnostic tasks. By analyzing the estimated stain abundances, we confirmed statistically significant differences in the relative stain abundances of EY and OG between the cytoplasmic mucins of EC and LEGH cells. Furthermore, in the classification of mucin patches from EC and LEGH cells, the proposed method achieved an accuracy of 98.0%, closely approaching the performance of MS-based stain unmixing (99.5%) and outperforming classifiers based on RGB, OD, and CIELAB features. These findings

suggest that stain unmixing not only enhances the interpretability of diagnosis but also improves classification accuracy. Recent studies have demonstrated that utilizing separated stain channels in H&E or IHC images can improve cell segmentation and classification (Pérez-Bueno et al., 2021; Ghahremani et al., 2022; Hu et al., 2022). As digital pathology continues to grow, stain unmixing is expected to play an increasingly significant role in enhancing the accuracy and reliability of computational cytology tools.

Nevertheless, several limitations of the current study merit discussion. First, the stain matrix was assumed to be shared across all images, based on measurements from single-stain reference samples. While this assumption simplifies implementation and ensures consistency, in practice, acquiring single-stain slides may not always be feasible. Second, all images used in this study were collected from a single institution, without accounting for potential color variations arising from differences in staining protocols, reagents, or imaging systems. Lastly, the current method focused on cropped regions of interest, and its applicability to WSIs remains to be explored.

Future work may focus on integrating adaptive or WSI-specific stain matrix estimation to better account for variability in staining conditions. We are also incorporating larger, more diverse datasets to enhance the generalizability of the proposed approach. In addition, expanding the range of downstream tasks based on stain abundance, such as morphological analysis and cell segmentation, would further demonstrate the utility of stain unmixing in digital pathology. Finally, investigating the practical deployment of the proposed method within real cytopathology workflows will be a critical step toward clinical translation.

Ethical approval

The experimental procedures involving human subjects described in this paper were approved by the Medical Ethics Committee of Shinshu University (Nov. 6, 2024, No. 5470).

CRedit authorship contribution statement

Nanxin Gong: Conceptualization, Investigation, Methodology, Software, Formal analysis, Visualization, Writing – original draft. **Saori Takeyama:** Investigation, Data curation, Software, Writing – review. **Masahiro Yamaguchi:** Conceptualization, Supervision, Project administration, Funding acquisition, Writing – review. **Takumi Urata:** Data curation, Validation. **Fumikazu Kimura:** Conceptualization, Validation, Resources, Supervision, Writing – review. **Keiko Ishii:** Validation, Resources, Writing – review.

Declaration of competing interest

The authors declare that they have no known competing financial interests or personal relationships that could have appeared to influence the work reported in this paper.

Acknowledgment

This work was supported by JST SPRING, Japan Grant Number JPMJSP2106 and JPMJSP2180, and Engineering Research Grants, Mizuho Foundation for the Promotion of Sciences. This paper was partly based on the results from project JPNP20006, subsidized by the New Energy and Industrial Technology Development Organization (NEDO).

Appendix A

In this appendix, we detail the proposed stain unmixing algorithm introduced in Section 3. We start by expanding the augmented Lagrangian introduced in (19):

$$\begin{aligned}
& L(\mathbf{X}, \mathbf{V}_1, \mathbf{V}_2, \mathbf{V}_3, \mathbf{V}_4, \mathbf{V}_5, \mathbf{D}_1, \mathbf{D}_2, \mathbf{D}_3, \mathbf{D}_4, \mathbf{D}_5) \\
&= \frac{1}{2} \|\mathbf{V}_1 - \mathbf{Y}\|_F^2 + \lambda \|\mathbf{W} \odot \mathbf{V}_2\|_{1,1} + \lambda_{TV} \|\mathbf{V}_4\|_{1,1} + \iota_{R^+}(\mathbf{V}_5) + \frac{\mu}{2} \|\mathbf{A}\mathbf{X} - \mathbf{V}_1 - \mathbf{D}_1\|_F^2 \\
&+ \frac{\mu}{2} \|\mathbf{X} - \mathbf{V}_2 - \mathbf{D}_2\|_F^2 + \frac{\mu}{2} \|\mathbf{X} - \mathbf{V}_3 - \mathbf{D}_3\|_F^2 + \frac{\mu}{2} \|\mathbf{H}\mathbf{V}_3 - \mathbf{V}_4 - \mathbf{D}_4\|_F^2 + \frac{\mu}{2} \|\mathbf{X} - \mathbf{V}_5 - \mathbf{D}_5\|_F^2 \quad (\text{A.11})
\end{aligned}$$

The ADMM iteratively minimizes $L(\mathbf{X}, \mathbf{V}, \mathbf{D})$ with respect to \mathbf{X} and \mathbf{V} followed by an update of \mathbf{D} in the following steps. Thus, we have

$$\mathbf{X}^{(k+1)} = (\mathbf{A}\mathbf{A}^T + 3\mathbf{I})^{-1} (\mathbf{A}^T(\mathbf{V}_1^{(k)} + \mathbf{D}_1^{(k)}) + (\mathbf{V}_2^{(k)} + \mathbf{D}_2^{(k)}) + (\mathbf{V}_3^{(k)} + \mathbf{D}_3^{(k)}) + (\mathbf{V}_5^{(k)} + \mathbf{D}_5^{(k)})) \quad (\text{A.2})$$

To compute the optimization for \mathbf{V} , we have

$$\mathbf{V}_1^{(k+1)} = \frac{1}{1 + \mu} [\mathbf{Y} + \mu(\mathbf{A}\mathbf{X}^{(k+1)} - \mathbf{D}_1^{(k)})]$$

$$\begin{aligned}
\mathbf{V}_2^{(k+1)} &= \text{soft}(\mathbf{X}^{(k+1)} - \mathbf{D}_2^{(k)}, \frac{\lambda}{\mu} \mathbf{W}) \\
\mathbf{V}_3^{(k+1)} &= (\mathbf{H}^T \mathbf{H} + \mathbf{I})^{-1} (\mathbf{X}^{(k+1)} - \mathbf{D}_3^{(k)} + \mathbf{H}^T (\mathbf{V}_4^{(k)} + \mathbf{D}_4^{(k)})) \\
\mathbf{V}_4^{(k+1)} &= \text{soft}(\mathbf{H} \mathbf{V}_3^{(k+1)} - \mathbf{D}_4^{(k)}, \frac{\lambda_{TV}}{\mu}) \\
\mathbf{V}_5^{(k+1)} &= \max(\mathbf{X}^{(k+1)} - \mathbf{D}_5^{(k)}, 0)
\end{aligned} \tag{A.3}$$

where $\text{soft}(\cdot, \tau)$ denotes the component-wise application of the soft-threshold function $y \mapsto \text{sign}(y) \max\{|y| - \tau, 0\}$. To compute the optimization for \mathbf{D} , we have

$$\begin{aligned}
\mathbf{D}_1^{(k+1)} &= \mathbf{D}_1^{(k)} - \mathbf{A} \mathbf{X}^{(k+1)} + \mathbf{V}_1^{(k+1)} \\
\mathbf{D}_2^{(k+1)} &= \mathbf{D}_2^{(k)} - \mathbf{X}^{(k+1)} + \mathbf{V}_2^{(k+1)} \\
\mathbf{D}_3^{(k+1)} &= \mathbf{D}_3^{(k)} - \mathbf{X}^{(k+1)} + \mathbf{V}_3^{(k+1)} \\
\mathbf{D}_4^{(k+1)} &= \mathbf{D}_4^{(k)} - \mathbf{H} \mathbf{V}_3^{(k+1)} + \mathbf{V}_4^{(k+1)} \\
\mathbf{D}_5^{(k+1)} &= \mathbf{D}_5^{(k)} - \mathbf{X}^{(k+1)} + \mathbf{V}_5^{(k+1)}.
\end{aligned} \tag{A.4}$$

References

- Abe, T., Murakami, Y., Yamaguchi, M., Ohyama, N., Yagi, Y., 2005. Color correction of pathological images based on dye amount quantification. *Opt Rev* 12, 293–300.
- Abousamra, S., Fassler, D., Yao, J., Gupta, R., Kurc, T., Escobar-Hoyos, L., Samaras, D., Shroyer, K., Saltz, J., Chen, C., 2023. Unsupervised stain decomposition via inversion regulation for multiplex immunohistochemistry images. *Proc Mach Learn Res* 227, 74.
- Bioucas-Dias, J.M., Figueiredo, M.A.T., 2010. Alternating direction algorithms for constrained sparse regression: Application to hyperspectral unmixing, in: 2010 2nd Workshop on Hyperspectral Image and Signal Processing: Evolution in Remote Sensing. pp. 1–4.
- Boyd, S., Parikh, N., Chu, E., Peleato, B., Eckstein, J., others, 2011. Distributed optimization and statistical learning via the alternating direction method of multipliers. *Foundations and Trends® in Machine learning* 3, 1–122.
- Chambolle, A., 2004. An algorithm for total variation minimization and applications. *J Math Imaging Vis* 20, 89–97.
- Chen, T., Srinivas, C., 2015. Group sparsity model for stain unmixing in brightfield multiplex immunohistochemistry images. *Computerized Medical Imaging and Graphics* 46, 30–39. <https://doi.org/10.1016/j.compmedimag.2015.04.001>
- Fassler, D.J., Abousamra, S., Gupta, R., Chen, C., Zhao, M., Paredes, D., Batool, S.A., Knudsen, B.S., Escobar-Hoyos, L., Shroyer, K.R., Samaras, D., Kurc, T., Saltz, J., 2020. Deep learning-based image analysis methods for brightfield-acquired multiplex immunohistochemistry images. *Diagn Pathol* 15. <https://doi.org/10.1186/s13000-020-01003-0>
- Fujii, K., Yamaguchi, M., Ohyama, N., Mukai, K., 2002. Development of support systems for pathology using spectral transmittance: the quantification method of stain conditions, in: *Medical Imaging 2002: Image Processing*. pp. 1516–1523.
- Gavrilovic, M., Azar, J.C., Lindblad, J., Wahlby, C., Bengtsson, E., Busch, C., Carlbom, I.B., 2013. Blind color decomposition of histological images. *IEEE Trans Med Imaging* 32, 983–994. <https://doi.org/10.1109/TMI.2013.2239655>

- Ghahremani, P., Li, Y., Kaufman, A., Vanguri, R., Greenwald, N., Angelo, M., Hollmann, T.J., Nadeem, S., 2022. Deep learning-inferred multiplex immunofluorescence for immunohistochemical image quantification. *Nat Mach Intell* 4, 401–412.
- Hu, H., Qiao, S., Hao, Y., Bai, Y., Cheng, R., Zhang, W., Zhang, G., 2022. Breast cancer histopathological images recognition based on two-stage nuclei segmentation strategy. *PLoS One* 17, e0266973.
- Iordache, M.-D., Bioucas-Dias, J.M., Plaza, A., 2012. Total variation spatial regularization for sparse hyperspectral unmixing. *IEEE Transactions on Geoscience and Remote Sensing* 50, 4484–4502.
- Iordache, M.-D., Bioucas-Dias, J.M., Plaza, A., 2011. Sparse unmixing of hyperspectral data. *IEEE Transactions on Geoscience and Remote Sensing* 49, 2014–2039.
- Ishii, K., 2001. A new diagnostic method for adenoma malignum and related lesions: latex agglutination test with a new monoclonal antibody, HIK1083. *Clin Chim Acta* 312, 231–233.
- Ishii, K., Katsuyama, T., Ota, H., Watanabe, T., Matsuyama, I., Tsuchiya, S., Shiozawa, T., Toki, T., 1999. Cytologic and cytochemical features of adenoma malignum of the uterine cervix. *Cancer Cytopathology: Interdisciplinary International Journal of the American Cancer Society* 87, 245–253.
- Jenkins, D., 2007. Histopathology and cytopathology of cervical cancer. *Dis Markers* 23, 199.
- Kai, M., Nunobiki, O., Taniguchi, E., Sakamoto, Y., Kakudo, K., 1999. Quantitative and qualitative analysis of stain color using RGB computer color specification. *Anal Quant Cytol Histol* 21, 477–480.
- Kanai, R., Ohshima, K., Ishii, K., Sonohara, M., Ishikawa, M., Yamaguchi, M., Ohtani, Y., Kobayashi, Y., Ota, H., Kimura, F., 2020. Discriminant analysis and interpretation of nuclear chromatin distribution and coarseness using gray-level co-occurrence matrix features for lobular endocervical glandular hyperplasia. *Diagn Cytopathol* 48, 724–735.
- Keshava, N., Mustard, J.F., 2002. Spectral unmixing. *IEEE Signal Process Mag* 19, 44–57.
- Kimura, F., Kobayashi, T., Kanai, R., Kobayashi, Y., Yuhi, O., Ota, H., Yamaguchi, M., Yokokawa, Y., Uehara, T., Ishii, K., 2019. Image quantification technology of the heterochromatin and euchromatin region for differential diagnosis in the lobular endocervical glandular hyperplasia. *Diagn Cytopathol* 47, 553–563.
- Macenko, M., Niethammer, M., Marron, J.S., Borland, D., Woosley, J.T., Guan, X., Schmitt, C., Thomas, N.E., 2009. A method for normalizing histology slides for quantitative analysis, in: 2009 IEEE International Symposium on Biomedical Imaging: From Nano to Macro. pp. 1107–1110.
- McRae, T.D., Oleksyn, D., Miller, J., Gao, Y.R., 2019. Robust blind spectral unmixing for fluorescence microscopy using unsupervised learning. *PLoS One* 14. <https://doi.org/10.1371/journal.pone.0225410>
- Nucci, M.R., 2014. Pseudoneoplastic glandular lesions of the uterine cervix: a selective review. *International Journal of Gynecological Pathology* 33, 330–338.
- Nucci, M.R., Clement, P.B., Young, R.H., 1999. Lobular endocervical glandular hyperplasia, not otherwise specified: a clinicopathologic analysis of thirteen cases of a distinctive pseudoneoplastic lesion and comparison with fourteen cases of adenoma malignum. *Am J Surg Pathol* 23, 886.

- Nunobiki, O., Sato, M., Taniguchi, E., Tang, W., Nakamura, M., Utsunomiya, H., Nakamura, Y., Mori, I., Kakudo, K., 2002. Color image analysis of cervical neoplasia using RGB computer color specification. *Anal Quant Cytol Histol* 24, 289–294.
- Pérez-Bueno, F., Serra, J.G., Vega, M., Mateos, J., Molina, R., Katsaggelos, A.K., 2022. Bayesian K-SVD for H and E blind color deconvolution. Applications to stain normalization, data augmentation and cancer classification. *Computerized Medical Imaging and Graphics* 97, 102048.
- Pérez-Bueno, F., Vega, M., Sales, M.A., Aneiros-Fernández, J., Naranjo, V., Molina, R., Katsaggelos, A.K., 2021. Blind color deconvolution, normalization, and classification of histological images using general super Gaussian priors and Bayesian inference. *Comput Methods Programs Biomed* 211, 106453.
- Rabinovich, A., Agarwal, S., Laris, C., Price, J., Belongie, S., 2003. Unsupervised color decomposition of histologically stained tissue samples. *Adv Neural Inf Process Syst* 16.
- Rossetti, B.J., Wilbert, S.A., Mark Welch, J.L., Borisy, G.G., Nagy, J.G., 2020. Semi-blind sparse affine spectral unmixing of autofluorescence-contaminated micrographs. *Bioinformatics* 36, 910–917. <https://doi.org/10.1093/bioinformatics/btz674>
- Rudin, L.I., Osher, S., Fatemi, E., 1992. Nonlinear total variation based noise removal algorithms. *Physica D* 60, 259–268.
- Ruifrok, A.C., Johnston, D.A., others, 2001. Quantification of histochemical staining by color deconvolution. *Anal Quant Cytol Histol* 23, 291–299.
- Sakamoto, Y., Taniguchi, E., Kakudo, K., 1998. Objective evaluation of Papanicolaou staining. *Anal Quant Cytol Histol* 20, 250–256.
- Takeyama, S., Watanabe, T., Gong, N., Yamaguchi, M., Urata, T., Kimura, F., Ishii, K., 2025. Dye amount quantification of Papanicolaou-stained cytological images by multispectral unmixing: spectral analysis of cytoplasmic mucin. *Journal of Medical Imaging* 12, 17501.
- Trahearn, N., Snead, D., Cree, I., Rajpoot, N., 2015. Multi-class stain separation using independent component analysis, in: *Medical Imaging 2015: Digital Pathology*. pp. 113–123.
- Vahadane, A., Peng, T., Sethi, A., Albarqouni, S., Wang, L., Baust, M., Steiger, K., Schlitter, A.M., Esposito, I., Navab, N., 2016. Structure-Preserving Color Normalization and Sparse Stain Separation for Histological Images. *IEEE Trans Med Imaging* 35, 1962–1971. <https://doi.org/10.1109/TMI.2016.2529665>
- Wang, R., Li, H.C., Pizurica, A., Li, J., Plaza, A., Emery, W.J., 2017. Hyperspectral Unmixing Using Double Reweighted Sparse Regression and Total Variation. *IEEE Geoscience and Remote Sensing Letters* 14, 1146–1150. <https://doi.org/10.1109/LGRS.2017.2700542>
- Weinstein, R.S., Graham, A.R., Richter, L.C., Barker, G.P., Krupinski, E.A., Lopez, A.M., Erps, K.A., Bhattacharyya, A.K., Yagi, Y., Gilbertson, J.R., 2009. Overview of telepathology, virtual microscopy, and whole slide imaging: prospects for the future. *Hum Pathol* 40, 1057–1069.
- Yagi, Y., 2011. Color standardization and optimization in whole slide imaging, in: *Diagnostic Pathology*. pp. 1–12.

Zhang, S., Li, J., Li, H.-C., Deng, C., Plaza, A., 2018. Spectral–spatial weighted sparse regression for hyperspectral image unmixing. *IEEE Transactions on Geoscience and Remote Sensing* 56, 3265–3276.

Zheng, Y., Jiang, Z., Zhang, H., Xie, F., Shi, J., Xue, C., 2019. Adaptive color deconvolution for histological WSI normalization. *Comput Methods Programs Biomed* 170, 107–120. <https://doi.org/10.1016/j.cmpb.2019.01.008>